Supplementary Information

Structural modulation enables magneto-dielectric effect and enhanced photoactivity in ferroelectric bismuth iron niobate pyrochlore

Shujie Sun,[*ab] Liuyang Zhu,[b] Bolin Zhang,[a] Lin Zhang,[a] Yuan Li,[a] Nian Cheng,[a] Xiaofeng Yin,[*a] Yongshang Tian,[*a] Xiaoning Li [c] and Yalin Lu [bd]

[a.] *Henan Collaborative Innovation Center of Energy-Saving Building Materials, Xinyang Normal University, Xinyang 464000, China.*

[b.] *CAS Key Laboratory of Materials for Energy Conversion, Department of Materials Science and Engineering, University of Science and Technology of China, Hefei 230026, China.*

[c.] *Institute for Superconducting and Electronic Materials, University of Wollongong, Wollongong 2500, Australia.*

[d.] *National Synchrotron Radiation Laboratory, University of Science and Technology of China, Hefei 230026, China.*

* *E-mail: sjsun@xynu.edu.cn; yxfeng@mail.ustc.edu.cn; tianyongshang@xynu.edu.cn*

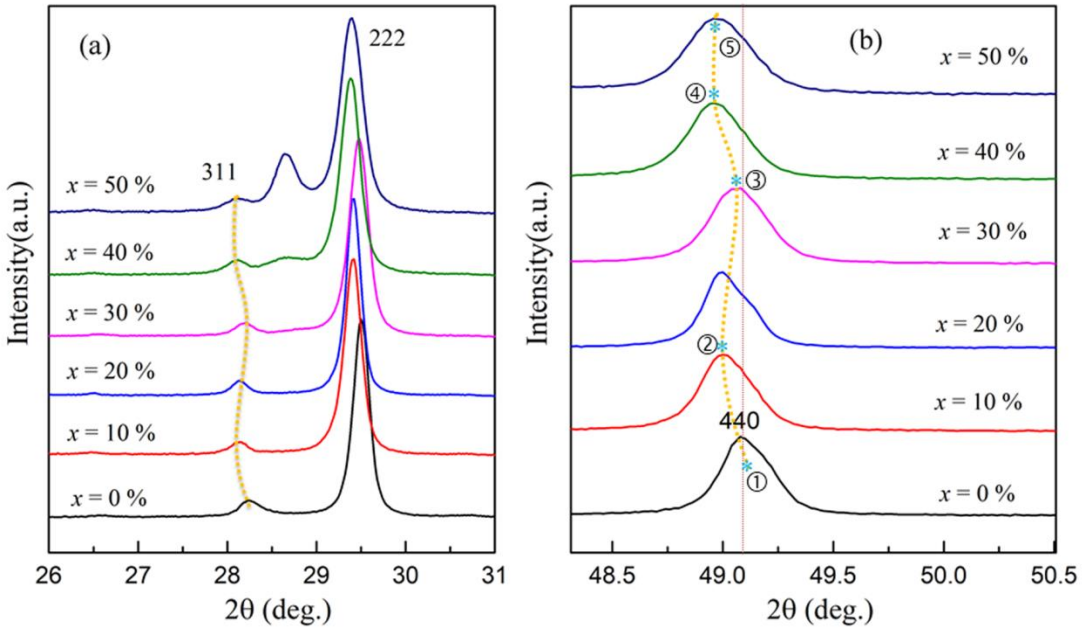

Fig. S1 Selected sections of the powder XRD patterns of the Bi-Fe-Co-Nb-O-x pyrochlores in the 2θ range of (a) 26° ~ 31° and (b) 48.1° ~ 50.5°**.** The peaks such as (311), (222) and (440) firstly shift toward the lower angle (①→②), then shift toward the higher angle (②→③), later shift toward the lower angle (③→④), and lastly keep nearly invariable (④→⑤), with increasing the amount of Co. This non-linear behaviour with respect to Co concentration might be explained as follows: 1)①→②, the ionic radius differences (Co^{2+} >Fe^{3+}) may generate lattice expansion or distortion; 2)②→③, it may exist the competing interactions between lattice distortion (improved) and structural disorder (suppressed), because that the change from the disorder to the ideal pyrochlore-type structure can give rise to a decreasing trend of lattice constant; 3)③→④, it may arise from the synergistic interactions between lattice distortion (improved) and structural disorder (improved); 4) ④→⑤, lattice structure may be tending to stability, attributing to the secondly phase. This analysis is very supported by the drastic change of the scatting intensity of the modes at 505cm^{-1} and 608cm^{-1}, as shown in Fig. S6.

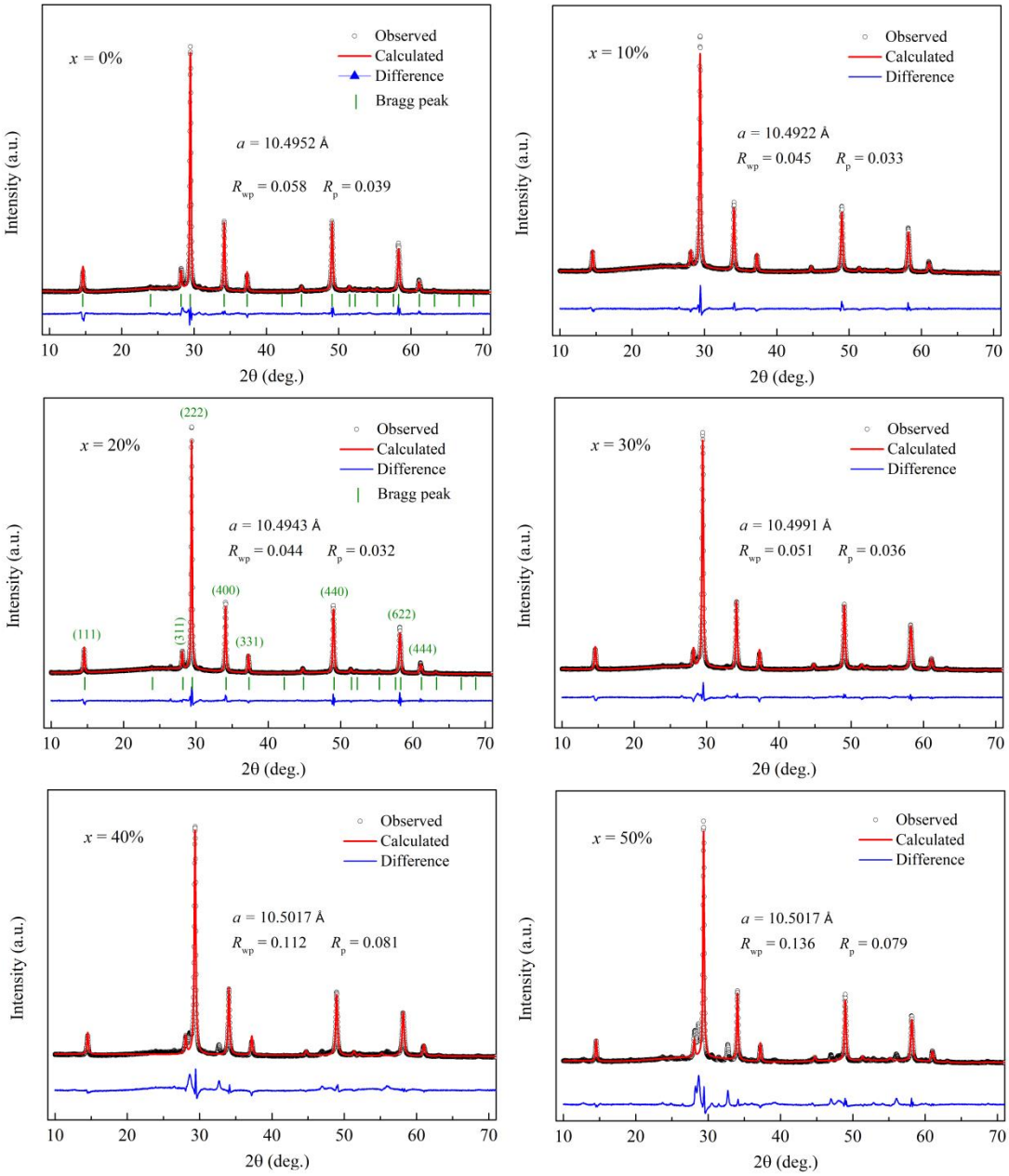

Fig. S2 Rietveld refinements for the powder XRD patterns of Bi-Fe-Co-Nb-O-x. These XRD patterns were refined in the cubic lattice using GSAS software. Circles indicate the experimental data and calculated data are the continuous black line overlapping them. The blue curve shows the difference between the experimental and calculated patterns. The vertical bars indicate the expected reflection positions.

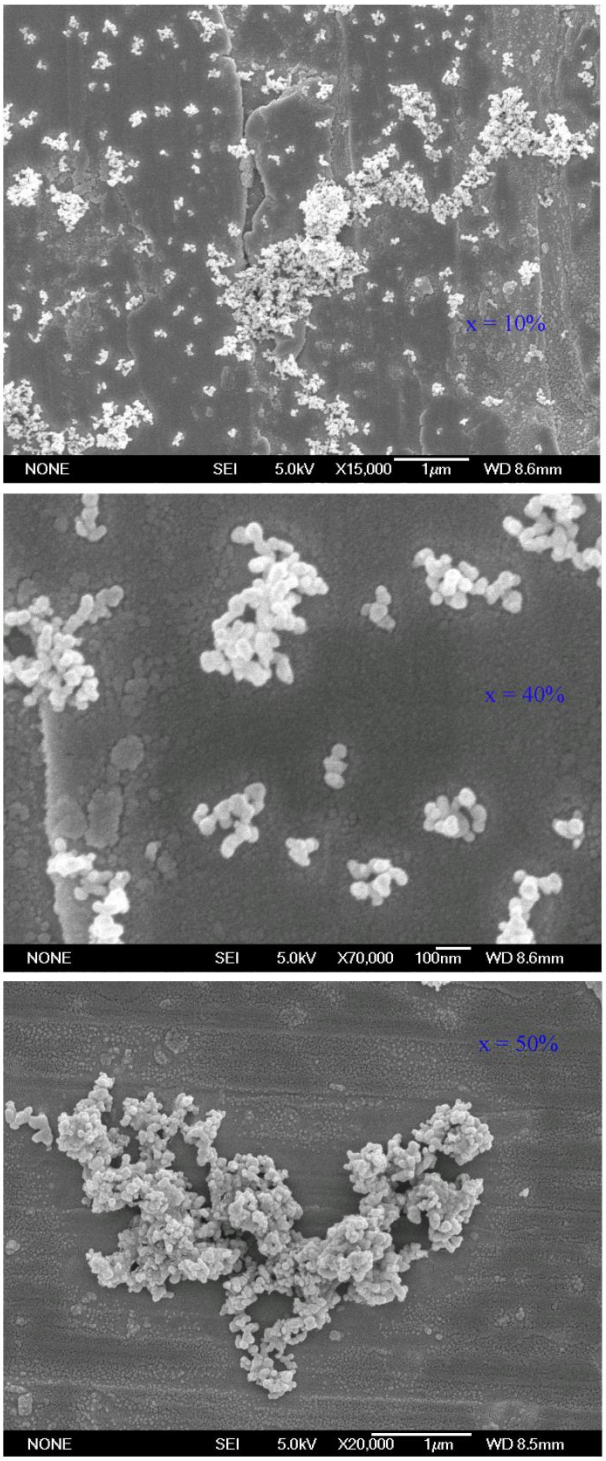

Fig. S3 SEM micrographs of Bi-Fe-Co-Nb-O-x (x = 10%, 40% and 50%).

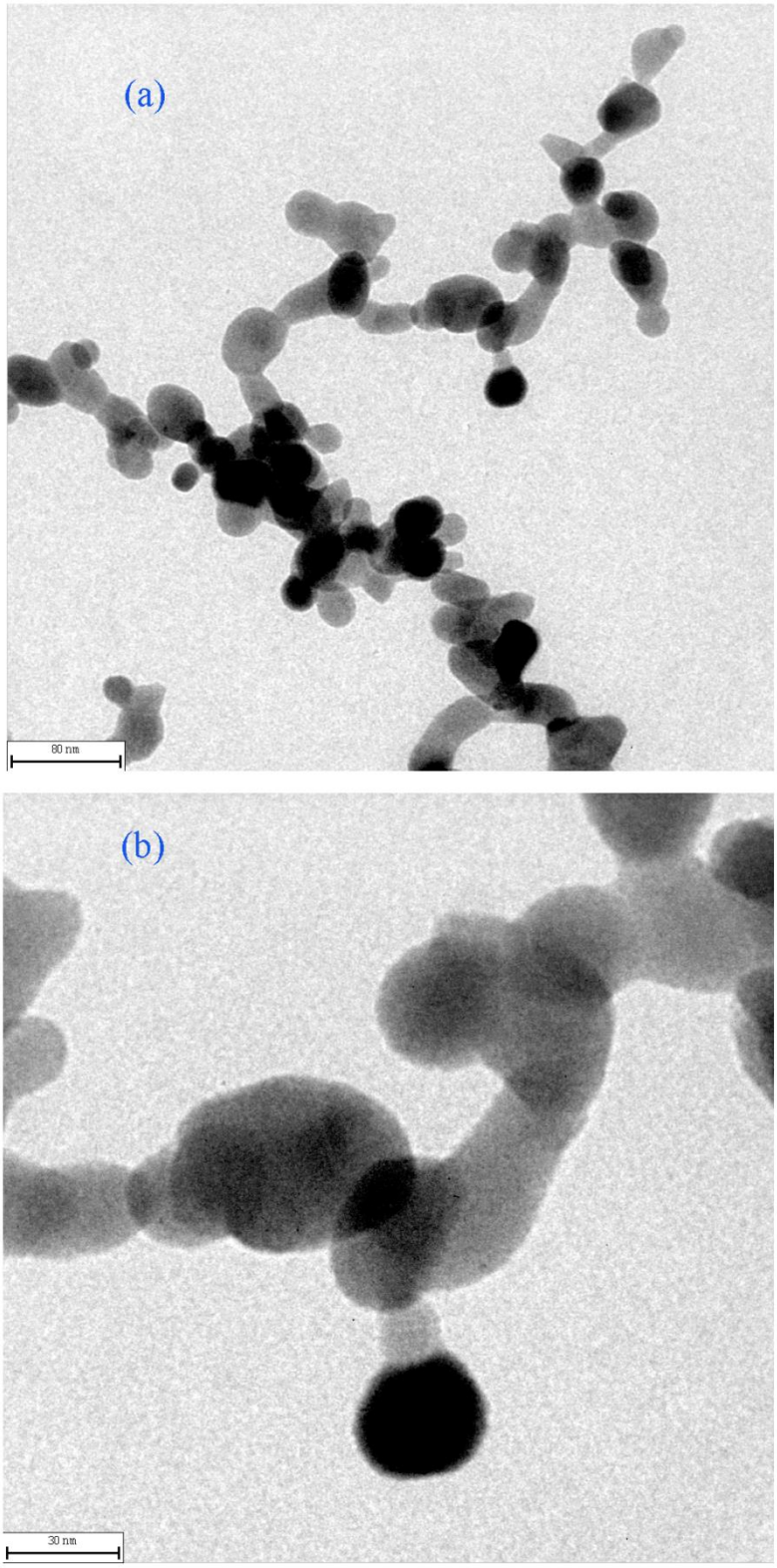

Fig. S4 (a) HRTEM image of the x = 20% sample. (b) Magnified HRTEM image.

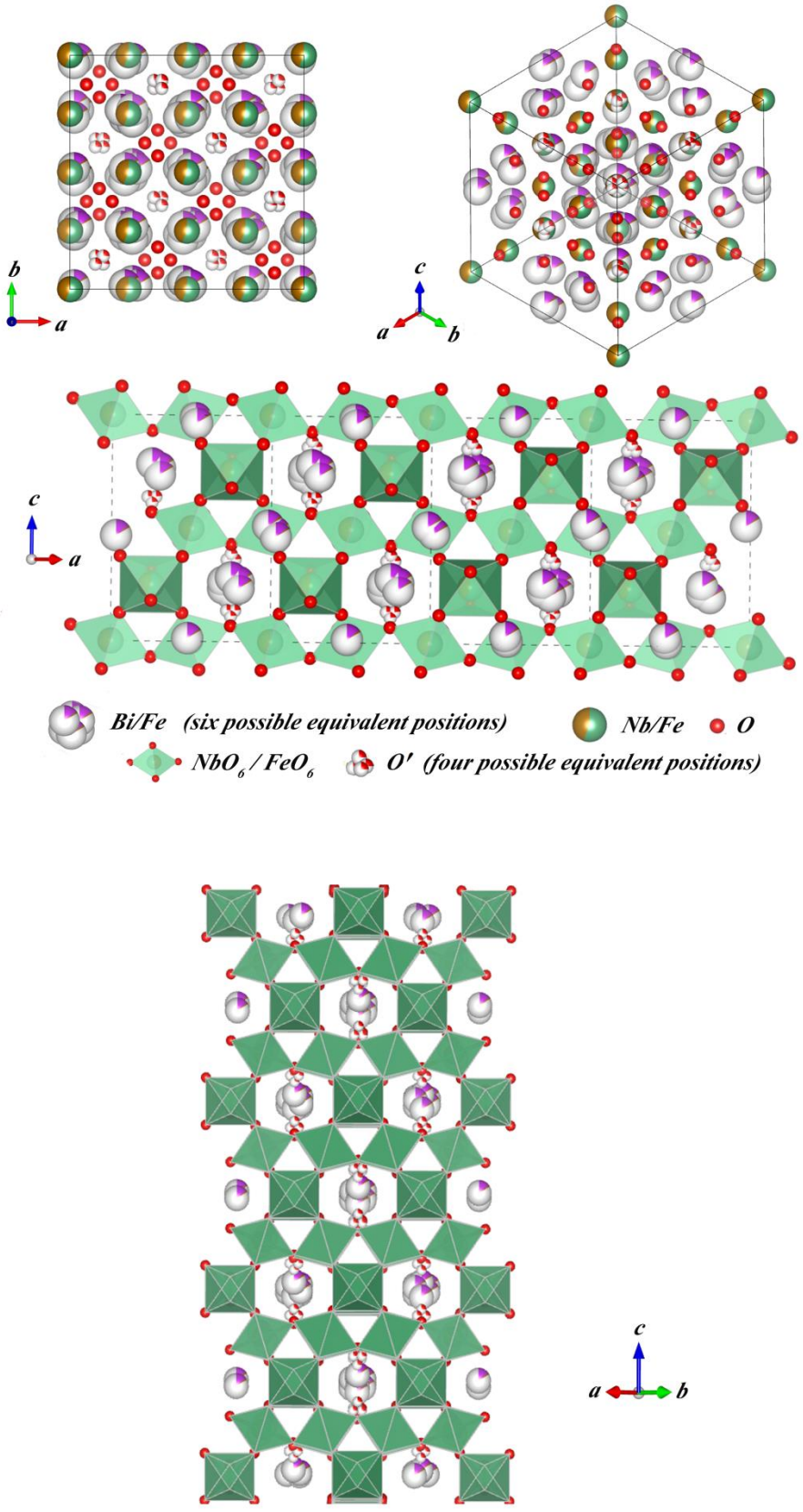

Fig. S5 Structure diagrams of $Bi_{1.721}Fe_{1.056}Nb_{1.134}O_7$ drawn using VESTA.

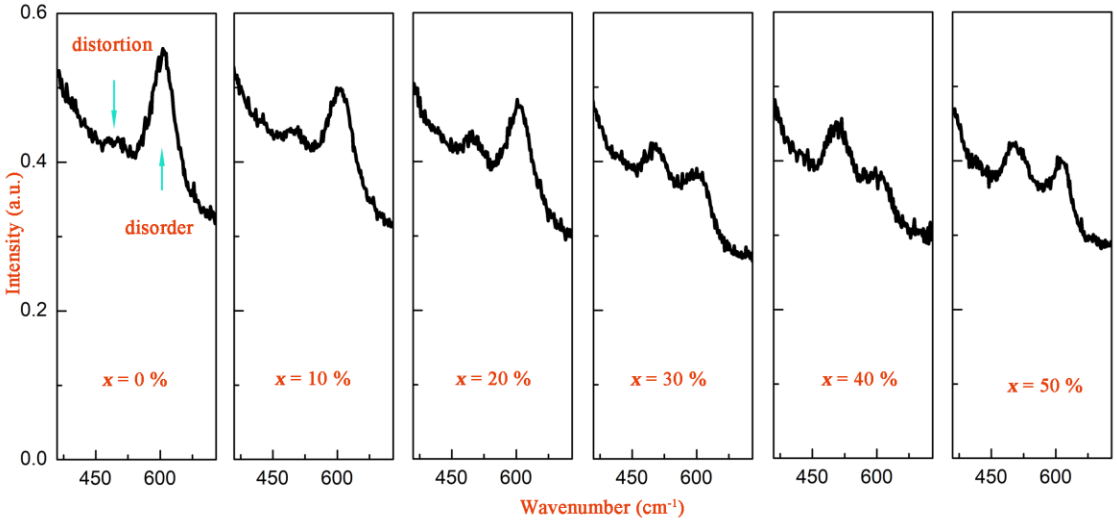

Fig. S6 Selected sections of Raman spectra of the Bi-Fe-Co-Nb-O-x at 360 cm^{-1} ~730 cm^{-1}. The intensities have been normalized. The scatting intensity of the modes at 505 cm^{-1} and 608 cm^{-1} present a drastic change, implying complicated interactions between lattice distortion and structural disorder in this system.

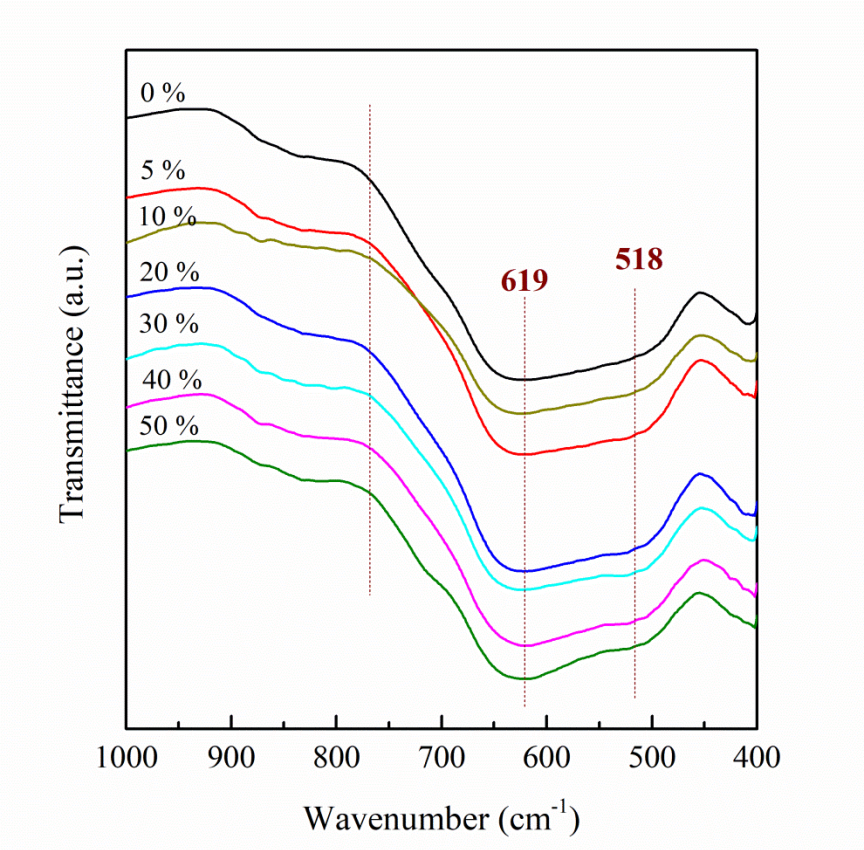

Fig. S7 Infrared spectra of Bi-Fe-Co-Nb-O-x in the 1000-400 cm^{-1}.

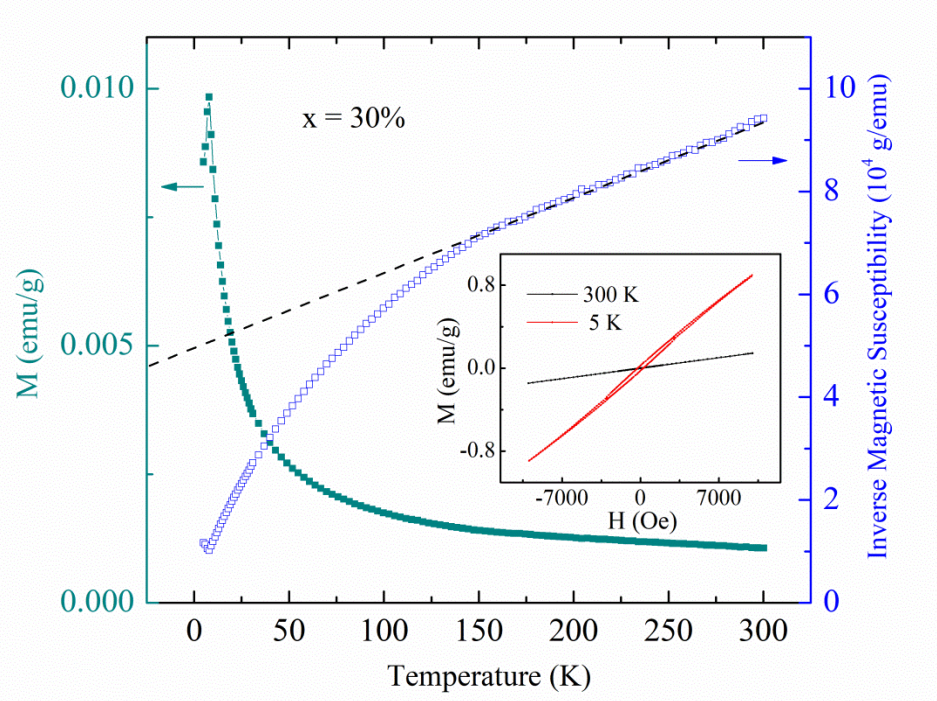

Fig. S8 Temperatuare dependence of the zero-field-cooled magnetic susceptibility and inverse magnetic susceptibility for x =30% at an applied field of 100 Oe. The inset shows the *M-H* loops for x = 30% at 5K and 300 K.

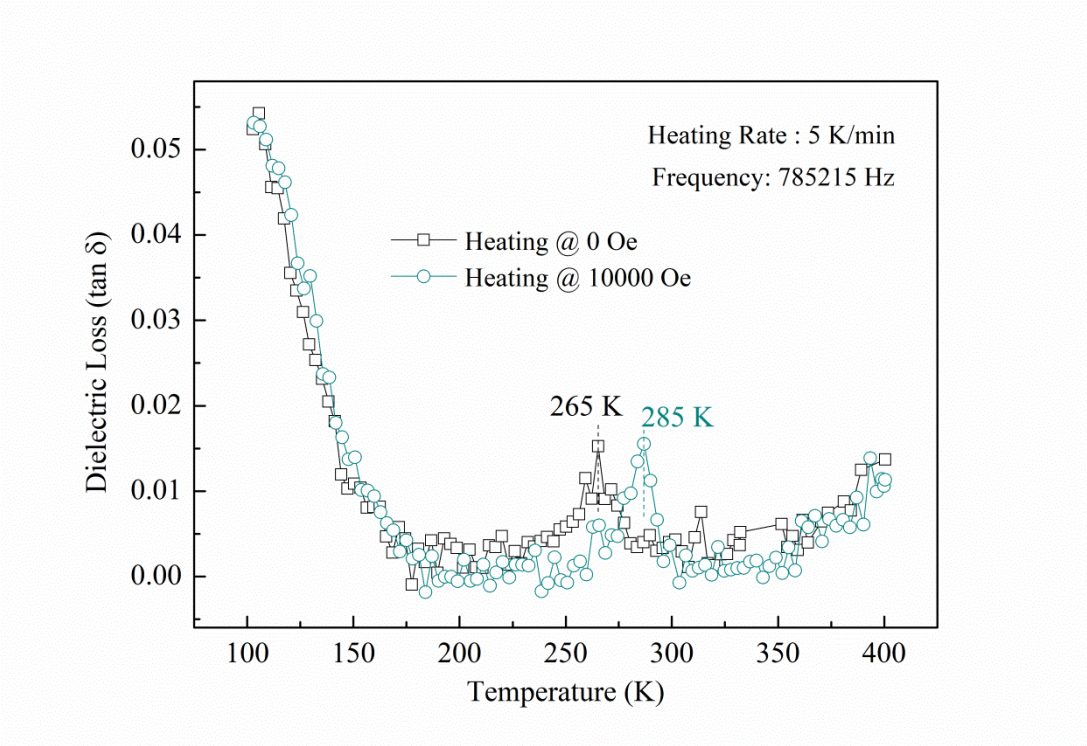

Fig. S9 Temperature dependence of the dielectric loss (tanδ) for x = 30% at the heating process at 785215 Hz under zero and 1 T magnetic fields.

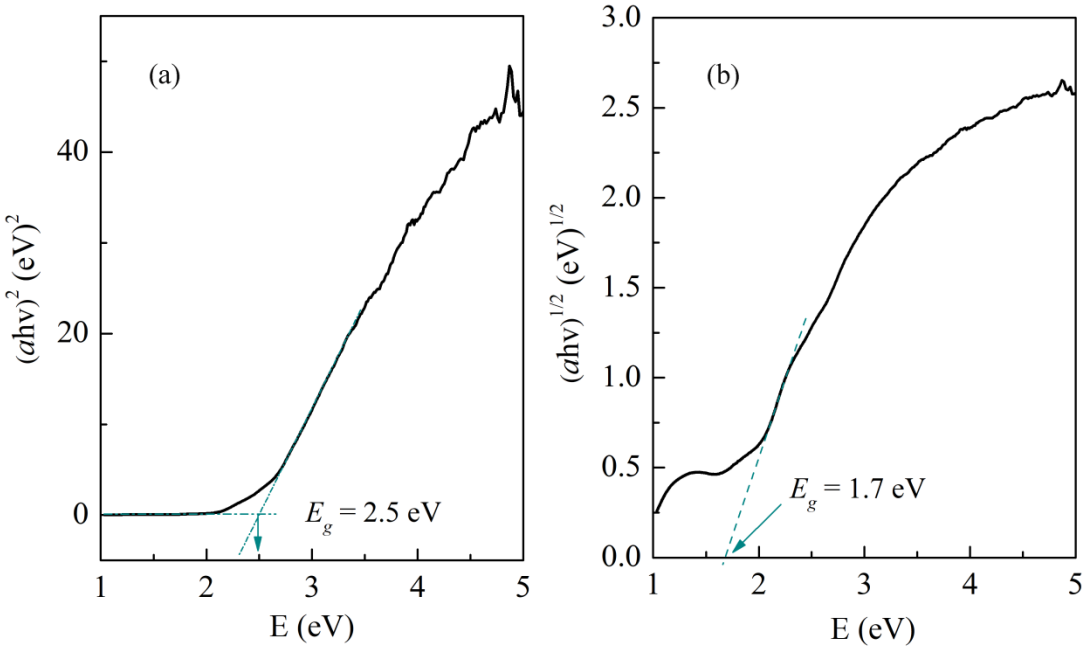

Fig. S10 Band gap energy of the un-doped sample (x = 0%) calculated by the Kubelka-Munk function for (a) direct and (b) indirect electron transition.

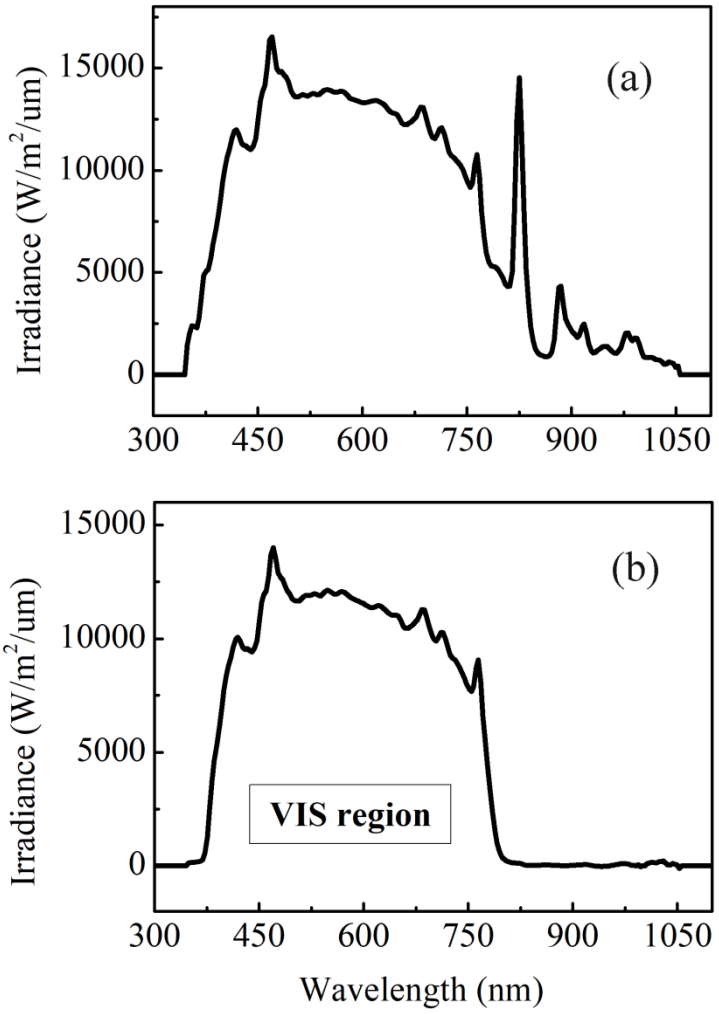

Fig. S11 (a) Spectral intensity of the photoreactor's light (a 300 W Xe lamp, PLX-SXE300). (b) Spectral intensity of the photoreactor's light with a filter (λ = 400-780 nm).

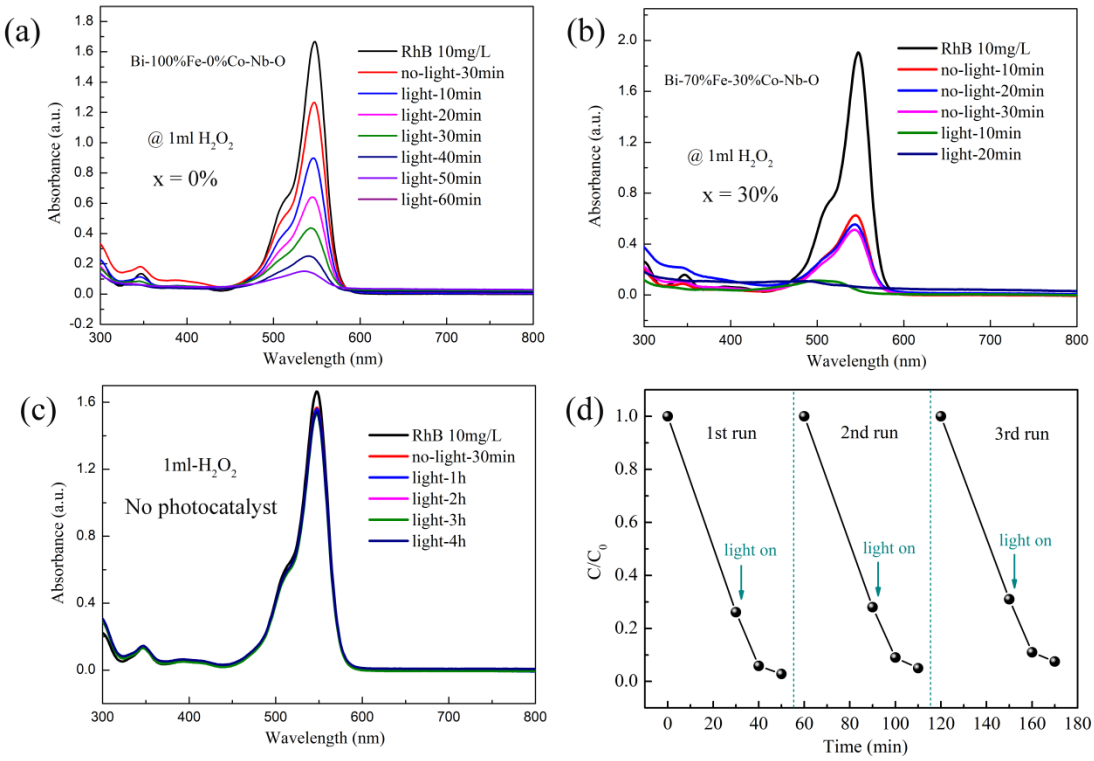

Fig. S12 Photodegradation of RhB using (a) Bi-Fe-Co-Nb-O-0%, (b) Bi-Fe-Co-Nb-O-30% and (c) no photocatalyst, with the addition of 1 ml 30% H_2O_2 aqueous solution as an electron scavenger. (d) Three photocatalytic degradation cycles of RhB using Bi-Fe-Co-Nb-O-30% as photocatalyst with the addition of 1 ml 30% H_2O_2 aqueous solution under visible-light irradiation.

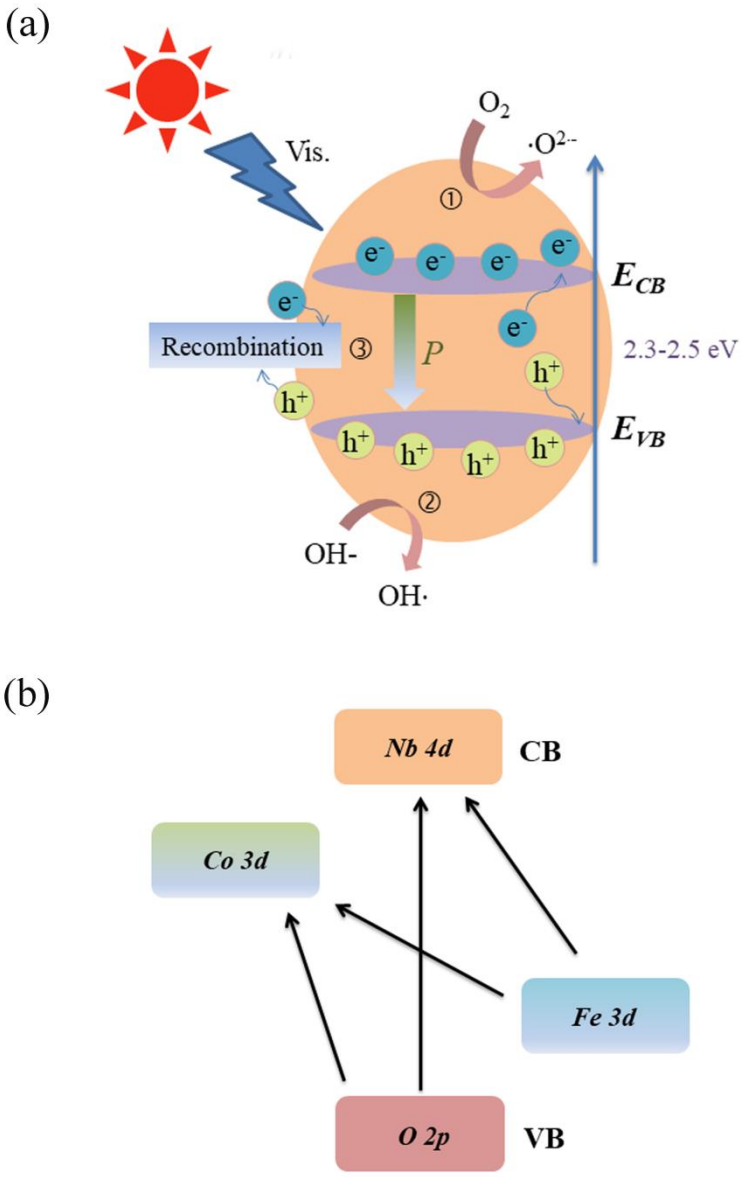

Fig. S13 (a) Plausible mechanism of photocatalytic degradation using Bi-Fe-Co-Nb-O-*x* photocatalysts. The Co-doped photocatalysts have wide absorbance and reduced band gap than that of the un-doped photocatalyst. More photo-excited electrons from the valance band (VB) of the Co-doped samples migrate to the conduction band (CB); later these photo-excited electrons that are accumulated on the surface were then trapped by the dissolved oxygen molecules in water to yield superoxide radical anions ($O_2\cdot^-$) and hydroxyl radicals (OH·). A possible role of ferroelectricity for the photocatalysis process is also shown in Figure

(a) and charge recombination events occur more easily on the surface of the photocatalysts. The effect of H_2O_2 is reflected on the behavior of $O_2\cdot^-$ and HO· produced in photocatalysis of Bi-Fe-Co-Nb-O-x. By the addition of H_2O_2, the reduction of O_2 by photoinduced conduction band electrons (e-) was increased was irradiated with visible light, since the consumption of photoinduced valence band holes (h^+) in the oxidation of H_2O_2 caused the repression of e^--h^+ recombination and the formation rate of HO· was increased. (b) Illustration of enhanced light absorption due to transition metal 3d state. The incorporation of Co will lower the conduction band edge by mixing Co-3d and Nd-4d. The valence band is the mixing of Fe-3d band with O-2p band. Therefore, the possible inter band transitions are illustrated.